Rybacki, E., Wirth, R., Dresen, G. (2010): Superplasticity and ductile fracture of synthetic feldspar deformed to large strain. - Journal of Geophysical Research, 115, B08209

DOI: 10.1029/2009JB007203

Superplasticity and ductile fracture of synthetic feldspar deformed to large strain

Erik Rybacki,[1] Richard Wirth,[1] and Georg Dresen[1]

Received 11 December 2009; revised 9 April 2010; accepted 30 April 2010; published 27 August 2010.

[1] We performed high-strain torsion experiments on fine-grained (≈4 μm) anorthite aggregates in a Paterson-type gas deformation apparatus. The dense hydrous (≈0.1 wt% H_2O) samples contain < 3 vol% Si-enriched residual glass located at triple junctions. Specimens were twisted at constant rate to a maximum shear strain of about 5 at experimental conditions of 100–400 MPa confining pressure, temperatures of 950°C–1200°C, and shear strain rates of ≈2×10^{-5}, 5×10^{-5}, and 2×10^{-4} s^{-1}. Resulting maximum shear stresses at the sample periphery were in the range of ≈2–80 MPa. The samples showed strain hardening at slow deformation rate and strain weakening at fast strain rate, respectively. Fitting the stress strain rate data to a power law yields linear viscous behavior. Microstructural analysis shows locally enhanced dislocation density, suggesting diffusion-assisted and/or dislocation-assisted grain boundary sliding as the dominant deformation mechanism. Deformed samples exhibit abundant cavities, nucleated mostly at grain triple junctions and at grain boundaries in response to cooperative grain boundary sliding. At shear strains ≥ 2, growth and coalescence of the cavities form an anastomozing network of regularly spaced strings oriented at about 30° to the direction of maximum compressive stress and ~15° to the shear plane. Strain is localized along these shear bands associated with a shape-preferred orientation of high-aspect ratio feldspar grains and with segregation of initial pore fluids (residual glass) into the bands. More than one third of the samples were deformed to terminal failure that occurred suddenly at shear strains of ≈3–5. The experiments indicate that cavitation damage may facilitate fluid flow and deep seismicity in highly strained shear zones.

Citation: Rybacki, E., R. Wirth, and G. Dresen (2010), Superplasticity and ductile fracture of synthetic feldspar deformed to large strain, *J. Geophys. Res.*, *115*, B08209, doi:10.1029/2009JB007203.

1. Introduction

[2] Creep tests performed on metals and ceramics at ambient pressure are often terminated by fracturing. Fracture mechanisms depend on temperature and applied stress and may be depicted in fracture mechanism maps analogous to creep deformation mechanism maps [*Ashby et al.*, 1979; *Gandhi and Ashby*, 1979]. At low temperature and high stress, the micromechanism of (brittle) fracture is dominated by cleavage and intergranular fracture associated with the nucleation and propagation of (preexisting) microcracks. At high temperature, the nucleation and growth of voids and cavities coupled with intracrystalline plasticity or diffusion processes lead to transgranular or intergranular creep fractures. Commonly, voids form at inclusions and second-phase particles, and cavitation refers to the formation of small pores along grain boundaries. The interaction of varying damage mechanisms leading to unstable rupture during high-temperature creep is still poorly understood in metals and ceramics and has not yet been investigated in detail in geological materials.

[3] Despite widespread evidence for dilatant crack damage and channeling of fluids in the deep crust and upper mantle [*Huenges et al.*, 1997], it is commonly assumed that elevated pressures suppress cavitation in mylonite shear zones [*Paterson*, 1990; *Landuyt and Bercovici*, 2009]. This inference is based on the observation on metal alloys where cavity nucleation and growth are suppressed at hydrostatic pressures on the order of the flow stress [*Bampton and Raj*, 1982; *Nicolaou and Semiatin*, 2003; *Pilling and Ridley*, 1988; *Zaki*, 1998]. In silicates, cavitation was observed in compression experiments performed at atmospheric pressures to axial strains > 10–20% [e.g., *Nair et al.*, 2001]. Cavitation at pressures significantly higher than the flow stress was first observed in synthetic fine-grained calcite samples using the split cylinder technique [*Walker et al.*, 1990] and in synthetic fine-grained anorthite-diopside aggregates, deformed by grain boundary sliding in torsion [*Dimanov et al.*, 2007].

[4] In nature, locally dilatant creep damage has been repeatedly suggested to occur in fine-grained high-strain ultramylonites [*White and White*, 1983; *Behrmann*, 1985; *Behrmann and Mainprice*, 1987; *Mancktelow et al.*, 1998;

[1]GFZ Potsdam, Potsdam, Germany.

0148-0227/10/2009JB007203

Table 1. Mechanical Data[a]

Sample	L_0 (mm)	ΔL (%)	T (°C)	P (MPa)	$\dot{\gamma}$ (s^{-1})	γ_{max}	τ_{max} (MPa)	n	Q (kJ mol^{-1})	Comment
Pl12_1	6.5	3.2	950	400	$1.7 \pm 0.3 \times 10^{-5}$	4.0	54	1.1 ± 0.6	257 ± 5	failure
Pl11_3	6.5	11.2	1000	400	$1.5 \pm 0.3 \times 10^{-5}$	4.0	22	0.8 ± 0.3	340 ± 62	
Pl38_1	6.5	2.3	1000	400	$1.7 \pm 0.1 \times 10^{-5}$	2.8	22			failure, 1 × back twist
Pl38_3	6.5	0.8	1000	400	$1.7 \pm 0.1 \times 10^{-5}$	2.8	32			failure, 2 × back twist
Pl11_2	6.5	16.5	1050	400	$1.4 \pm 0.3 \times 10^{-5}$	3.9	12	0.9 ± 0.2	282 ± 32	
Pl01_b	10	1.6	1050	400	$5.9 \pm 0.1 \times 10^{-5}$	4.3	70	0.9		failure
Pl10_1	6.5	9.5	1100	400	$1.6 \pm 0.1 \times 10^{-5}$	4.2	11	1.0 ± 0.1	425 ± 52	
Pl12_3	6.0	4.2	1100	400	$4.5 \pm 0.3 \times 10^{-5}$	3.4	24.5	0.8 ± 0.1	401 ± 28	failure
Pl10_3	6.5	1.2	1100	400	$2.3 \pm 0.0 \times 10^{-4}$	3.2	55	0.8 ± 0.1	321 ± 18	failure
Pl01_a	10	0.6	1100	400	$2.0 \pm 0.1 \times 10^{-4}$	3.3	59	0.8 ± 0.1	328 ± 25	axial deformation
Pl02_b	10	0.5	1100	400	$2.0 \pm 0.1 \times 10^{-4}$	3.4	77	1.1 ± 0.1	378 ± 53	axial deformation
PlT6_3	5.0	2.1	1100	100	$1.7 \pm 0.1 \times 10^{-5}$	2.3	73			failure
PlT6_2	5.0	2.0	1100	250	$1.7 \pm 0.1 \times 10^{-5}$	4.4	73			failure
PlT6_1	5.0	2.1	1100	400	$1.7 \pm 0.1 \times 10^{-5}$	2.2	63			slipped
PlT6_4	5.0	2.2	1100	400	$1.7 \pm 0.1 \times 10^{-5}$	3.4	78			failure
Pl09_1	6.5	16.5	1125	400	$1.5 \pm 0.5 \times 10^{-5}$	3.8	7.2	1.4 ± 1.1	378 ± 58	
Pl09_2	4.0	15.0	1125	400	$1.4 \pm 0.3 \times 10^{-5}$	4.1	5.9	0.8 ± 0.2	436 ± 20	
Pl09_3	3.0	8.7	1125	400	$1.6 \pm 0.3 \times 10^{-5}$	4.4	3.9	0.8 ± 0.1	485 ± 40	
Pl09_4	2.0	4.0	1125	400	$1.7 \pm 0.1 \times 10^{-5}$	4.8	6.7	0.7 ± 0.1	264 ± 21	
Pl09_5	1.0	−3.0	1125	400	$1.8 \pm 0.1 \times 10^{-5}$	2.7	14	1.1 ± 0.1	262 ± 23	
Pl38_2	1.0	−7.0	1125	400	$1.9 \pm 0.1 \times 10^{-5}$	5.6	5.3	0.9 ± 0.2	330 ± 13	
Pl10_2	6.5	8.3	1150	400	$1.5 \pm 0.1 \times 10^{-5}$	4.3	5.5	0.8 ± 0.2	404 ± 81	
Pl12_2	6.5	0.0	1150	400	$1.5 \pm 0.0 \times 10^{-4}$	3.4	27	0.8 ± 0.1	461 ± 13	failure
Pl11_1	6.5	5.1	1200	400	$1.6 \pm 0.1 \times 10^{-5}$	4.3	1.5	0.9 ± 0.3	438 ± 34	
Pl02_a	10	1.3	1200	400	$2.0 \pm 0.1 \times 10^{-4}$	4.4	35	1.0 ± 0.1	480 ± 40	

[a] L_0 is initial length, ΔL is maximum elongation, T is temperature, $\dot{\gamma}$ is maximum shear strain rate, γ_{max} is maximum strain, n is average stress exponent, and Q is average activation energy calculated from twist rate and temperature steppings.

Zavada et al., 2007]. It is conceivable that cavitation may contribute to an enhanced permeability and fluid flow localized in shear zones that is frequently observed [*Rutter and Brodie*, 1985]. Unstable ductile failure in mylonite shear zones at the base of the seismogenic upper crust has been suggested as a possible source mechanism for earthquakes [*Hobbs and Ord*, 1988] and pseudotachylytes at great depth [*Austrheim and Boundy*, 1994; *Hobbs et al.*, 1986; *White*, 1996; *Renshaw and Schulson*, 2004]. Failure is often attributed to shear heating and/or dehydration reactions and possibly transient fluid pressure pulses. Strain-dependent accumulation of locally dilatant creep damage leading to failure may provide an alternative mechanism.

[5] Here we focus on the rheology of feldspar aggregates. Feldspar forms the major mineral constituent of rocks in the lower continental crust. Several experimental studies were recently conducted to examine the high-temperature rheology of fine-grained pure feldspar aggregates [*Tullis and Yund*, 1991; *Tullis et al.*, 1996; *Dimanov et al.*, 1998; *Dimanov et al.*, 1999; *Rybacki and Dresen*, 2000; *Rybacki et al.*, 2006]. These previous experiments were performed in triaxial compression at low axial strain < 30%. At these low strains, cavitation or ductile failure was never observed. However, highly strained feldspar samples show strong cavitation and rearrangement of pore fluids leading to catastrophic failure [*Rybacki et al.*, 2008]. Here we describe in detail the results of torsion experiments on fine-grained synthetic anorthite aggregates, deformed to high strain comparable to those attained in natural mylonites.

2. Starting Material

[6] Samples were fabricated using a commercially available, fine-grained anorthite (An_{99}) glass powder (grain size $d < 11\mu m$) containing less than 1% impurities (Schott-Glaswerke, Germany). The predried powder (dried for 60 h at 800°C in air) was first cold-pressed at 170 MPa axial stress into iron canisters of 14 mm diameter and 30 mm length. Pellets (Pl01, Pl02, Pl09–Pl12, and Pl38) were then isostatically hot-pressed at $P = 300$ MPa confining pressure and $T = 880$°C temperature for 0.5 h and subsequently at $T = 1100$°C for 24 h. A second sample batch (PlT6) was first hot-pressed at 900°C for 2 h, followed by 20 h at 1150°C, using powder predried for 60 h at 800°C in argon. This glass-ceramics approach resulted in fine-grained and dense aggregates (porosity ≈ 1%). After removing the jacket by dissolving in acid, the aggregates were ground and polished to obtain cylindrical samples of 10 mm diameter and a length between 1 and 10 mm (Table 1).

[7] The grain size of undeformed specimens was measured with the line intercept method on thermally etched sections (1100°C for 60 h) and analyzed with a scanning electron microscope (SEM, Zeiss DSM 962). Grains are often prismatic with an aspect ratio of about 2.5. The mean grain size is $d = 3.7 \pm 0.7$ μm, calculated from mean intercept length and using a stereological correction factor of 1.9 [*Underwood*, 1970]. Ultrathin sections show a homogeneous distribution of grains within samples Pl01, Pl02, and PlT6, while samples Pl09–Pl12 and Pl38 reveal a shape-preferred orientation of grains in spherulite-like domains of about 1–2 mm in size. Optical inspection of these domains with crossed polarizers and compensated by a gypsum plate indicates a crystallographic-preferred orientation (texture) within the domains. Transmission electron microscope (TEM, Fei Tecnai™G^2 F20 X-twin) observations on focused ion beam (FIB) thinned sections show twins, low dislocation densities ($<10^{12}$ m^{-2}) including some subgrain boundaries formed by dislocation arrays, locally antiphase boundaries, and few fluid inclusions. Less than 3 vol% Si-enriched residual glass containing typically > 90 wt% SiO_2 is located in grain triple

junctions and surrounding some fluid inclusions. Within spherulitic domains, the glass partially wets grain boundaries. The water content of samples predried in air is ≈0.17 ± 0.04 wt% H_2O and that from the second batch predried in argon is ≈0.08 ± 0.02 wt% H_2O. Water content was estimated with Fourier-transformed infrared spectroscopy (FTIR, Bruker IFS-66v) using a molar extinction coefficient of 32 $l_{(H_2O)}$ $mol^{-1}cm^{-1}$. The broad absorbance spectra indicate water incorporated mainly as molecular H_2O and hydroxyl groups. The spot size of the infrared beam is about 60 μm diameter and larger than the average grain size. This precludes estimating water content in the grain interior. We expect higher water content along grain boundaries based on measurements of embedded anorthite single crystals in similar starting material [*Rybacki et al.*, 2006]. "Wet" samples are assumed to be water-saturated at experimental conditions. Further details of sample preparation and characterization are described in the works of *Rybacki and Dresen* [2000] and *Rybacki et al.* [2006]. The water content of starting material and deformed samples was similar within error bars, indicating that no water was lost during the runtime of the experiments.

3. Experimental Procedure

[8] We performed high-strain torsion experiments on 26 samples at constant twist rate in a Paterson-type gas deformation apparatus at 100–400 MPa confining pressure. A total of 19 specimens was twisted at a peripheral shear strain rate of ≈1.7 × 10^{-5} s^{-1}, two samples at ≈5 × 10^{-5} s^{-1}, and five samples at ≈2 × 10^{-4} s^{-1} in a temperature range of 950°C–1200°C (Table 1).

[9] The calculation of maximum shear stress and shear strain (rate) at the outer sample surface from measured torque and twist data taking into account sample elongation follows the procedures described by *Paterson and Olgaard* [2000] and *Rybacki et al.* [2003]. We estimated stress exponent n and activation energy Q from stress and temperature stepping tests, respectively. We assume that the deformation behavior of the water-saturated rocks can be fit to a power law of the form

$$\dot{\gamma} = A\tau^n \exp\left(-\frac{Q+pV}{RT}\right) d^{-m} f_{H_2O}^{p}, \quad (1)$$

where $\dot{\gamma}$ is shear strain rate (s^{-1}), A is a material-dependent constant (MPa^{-n-p} μm^m s^{-1}), τ is shear stress (MPa), n is stress exponent, Q is activation energy (kJ mol^{-1}), p is pressure (MPa), V is activation volume (μm^3 mol^{-1}), R is molar gas constant (kJ mol^{-1} K^{-1}), T is absolute temperature (K), d is grain size (μm), m is grain size exponent, f_{H_2O} is water fugacity (MPa), and p is fugacity exponent.

[10] To calculate stress and temperature sensitivity n and Q, respectively, we performed one to three twist rate and temperature steppings during most runs. Twist rate was increased or decreased three to four steps up to a factor of 4, and temperature was stepped up or down 2–4 times in intervals of 10°C–20°C. In addition, most samples were unloaded and reloaded 1–5 times per run at a given strain rate to correct data for a latent zero-drift of the torque cell and to measure axial hit points to determine changes of sample length. Six specimens with initial lengths between 1 and 6.5 mm (Pl09_1.5, Pl38_2) were deformed at similar conditions to evaluate a potential effect of specimen length on elongation and localization. Two samples (Pl38_1 and Pl38_3) were twisted back and forth, respectively, to study the evolution of stress and microstructure upon reversing the shear direction. To compare sample strength under different loading conditions, two other samples (Pl01_a, Pl02_b) were deformed axially after twisting.

[11] All samples were jacketed in iron sleeves with ≈0.34 mm wall thickness. Measured torque and angular displacement (axial force and displacement) were corrected for jacket strength and system compliance by means of calibration experiments on dummy specimens from similar material. The error in the measurement of the stress is about 4%, of the strain ≈1%, and of the temperature ≈0.3%, owing to precision of sensors and conversion procedures. The strain rate decreases with increasing strain due to sample elongation. The decrease in strain rate varies from ≈3% for specimens with a total elongation of ≈1% to about 40% for a sample with 16.5% elongation. Heating and cooling rates were 30°C/min, and samples were cooled to room temperature under torque for microstructural investigations.

4. Results

4.1. Stress-Strain Behavior

[12] Samples were deformed to maximum shear strains between 2.8 and 5.6, supporting maximum shear stresses between 1.5 and 77 MPa (Table 1). For conversion of measured torque to shear stress we used a mean stress exponent of $n = 1.1$ as determined from twist rate stepping tests (Table 1). About 40% of the samples were deformed to terminal failure. No strain weakening was observed prior to failure. At temperatures < 1200°C, specimens deformed at low strain rate (≈1.6 × 10^{-5} s^{-1} and ≈5 × 10^{-5} s^{-1}) show continuous hardening with increasing strain (Figures 1a, 1b, and 1f). Samples deformed at high strain rate (≈2 × 10^{-4} s^{-1}) commonly reveal steady state behavior or a slight weakening with increasing strain (Figure 1c). Strength and strengthening/weakening rate decrease with increasing temperature.

[13] As expected, for all but one sample, the mechanical behavior was not affected by the initial sample length, suggesting that end effects (friction, elastic distortion [e.g., *Paterson and Wong,* 2005]) are negligible for fine-grained specimens with length > 1 mm (Figure 1d). Reversing the shear sense after a shear strain of about 2.8 results in a considerable increase of strength and hardening rate (Figure 1e, dashed line, sample Pl38_1). This effect is even more pronounced upon repeated twist reversal (solid line, sample Pl38_3). Sample strength and the shape of stress-strain curves do not depend on the applied confining pressure in the range of 100–400 MPa (Figure 1f). Note that samples prepared from the second batch containing less water (PlT6_1–PlT6_4) are noticeably stronger than those fabricated from the first batch.

[14] Two cylindrical samples (Pl01_a, Pl02_b) of 10 mm length × 10 mm diameter were deformed in axial compression subsequent to twisting to a shear strain of $\gamma \approx 3.4$. At first, samples were axially shortened at constant load to ≈7% axial strain and then at constant displacement rate to ≈32% total axial strain until steady state stresses were achieved. To compare data from axial compression and torsion tests, shear stress and shear strain measured in torsion were converted to

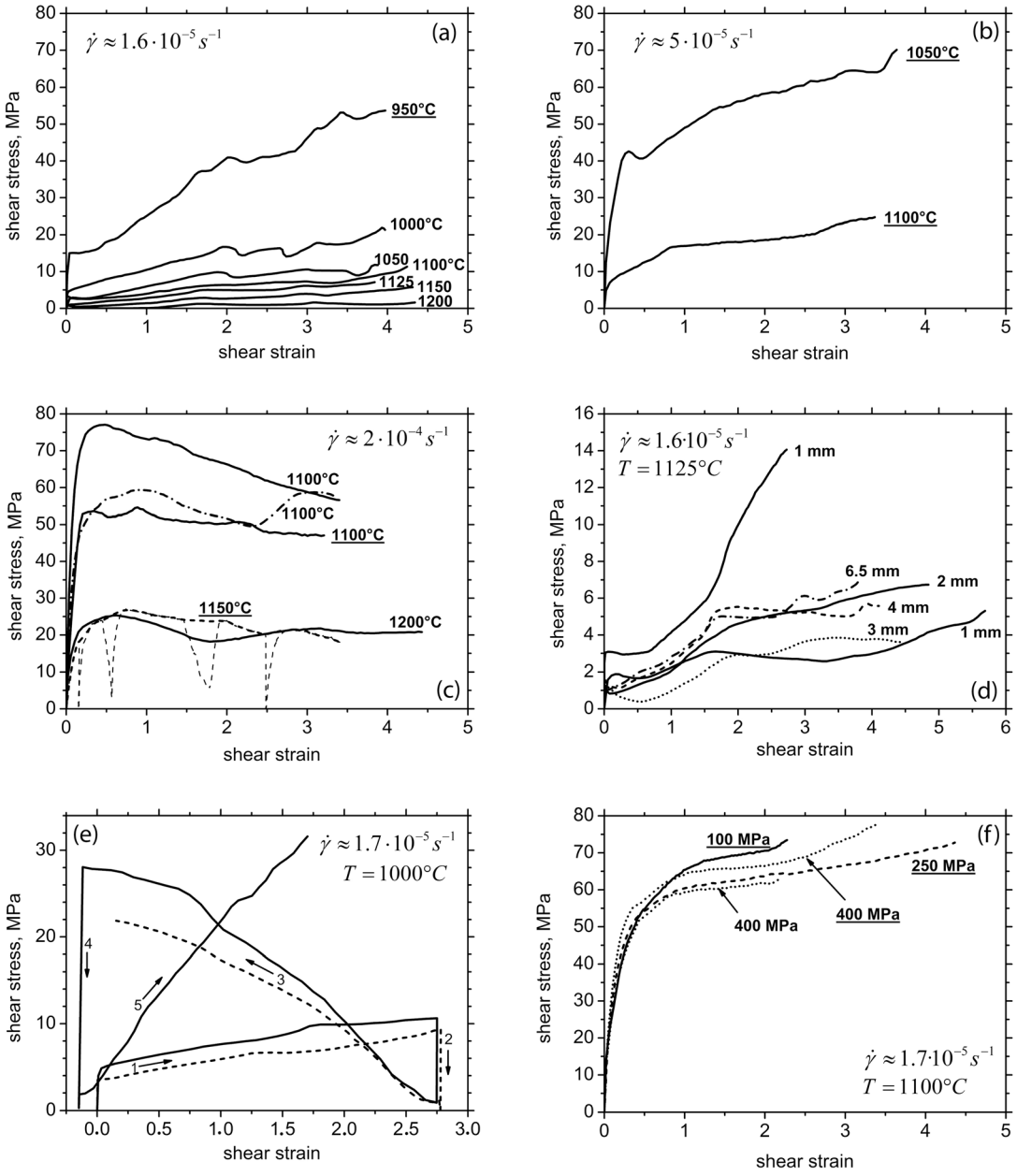

Figure 1. Smoothed stress-strain curves of anorthite samples deformed in torsion at 400 MPa confining pressure. The variations of strength with (a–c) temperature at three different strain rates, (d) sample length, (e) reversal of twist sense, and (f) confining pressure. Samples that failed before deformation was stopped are indicated by underlined temperature labels at each curve. All stress-strain curves shown represent smoothed curves for which the twist rate, temperature, and unloading cycles are erased for legibility. An example of a complete curve including twist rate and temperature steppings is shown in thin dashed line in Figure 1c. Test conditions are labeled in each plot. Samples shown in Figure 1f contain less water than other samples.

equivalent stress and strain assuming a von Mises yield criterion [e.g., *Paterson and Olgaard*, 2000]. The data from the two samples deformed both in torsion and compression are in good agreement within sample to sample variation and indicate a stress exponent of $n \approx 1$ (Figure 2).

4.2. Flow Law Parameters

[15] Mean stress exponent n and activation energy Q (Table 1) were determined from twist rate and temperature steppings. Values represent an average of three to four individual steps at low, intermediate, and high strain, respectively. The low standard deviations for n (±20%) and Q (±10%) show that these parameters remained rather unchanged with increasing strain. However, the activation energies estimated from temperature steps show a large scatter between samples, ranging from 257 to 485 kJ mol^{-1} (Table 1). The Q values appear to increase with temperature by about 75 kJ mol^{-1} per 100°C. This may reflect an

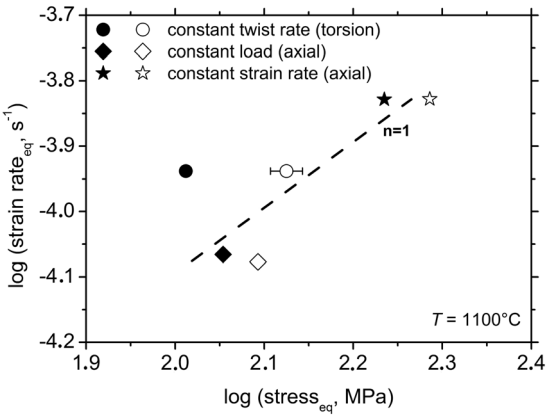

Figure 2. Steady state equivalent stress–equivalent strain rate values in log-log scale for two samples deformed at first in torsion, then at constant load in triaxial compression, and finally at constant axial deformation rate (solid symbols, sample Pl01_a; open symbols, sample Pl02_b). Dashed line indicates a stress exponent of 1.

increasing contribution of grain boundary dislocation activity with increasing temperature, although the stress exponent remains close to 1. Significant dislocation accommodation at high strains was observed in linear viscous creep of anorthite-diopside mixtures [*Dimanov et al.*, 2007]. The mean stress exponent of all samples is 0.9 ± 0.3 and the mean activation energy is 371 ± 76 kJ mol^{-1}.

[16] We estimated n and Q also by comparing torsion test data from different samples at a similar strain of $\gamma = 3$ (Figure 3). The resulting mean stress exponent is $n = 1.1 \pm 0.2$, which is similar to the value obtained using stepping tests performed on individual samples (Figure 3a). The mean activation energy is $Q = 202 \pm 47$ kJ mol^{-1}, which is in good agreement with the value of 170 ± 6 kJ mol^{-1} obtained by *Rybacki and Dresen* [2000] on similar material in triaxial compression tests (Figure 3b).

4.3. Sample Elongation

[17] For plastic deformation in torsion, the geometry of samples should remain constant to large strain. However, microstructural effects like a change of porosity, metamorphic reactions, or the evolution of a lattice- or shape-preferred orientation may affect the sample shape with progressive strain. In most experiments, we measured the length of samples in strain intervals of $\gamma \approx 1.5$ by unloading and determining the axial touch point and final length after deformation. Samples with initial length ≥ 6.5 mm elongate up 16.5% with strain, in particular beyond $\gamma \geq 1.5$–2.0 (Figure 4 and Table 1). The increase of length appears less pronounced at high strain rate and high stress irrespective of temperature (Figures 4a and 4b), associated with minor strain hardening at high strain rate. Sample elongation decreases with decreasing initial length of < 4 mm. For 1 mm thick samples, we observed up to 7% shortening (Figure 4c). Samples also shorten upon reversal of the shear sense (Figure 1e) and when subjected to a small axial load of ≤ 1 MPa during twisting (Figure 4d).

4.4. Macroscopic Deformation

[18] During deformation the diameter of most samples was progressively reduced with increasing elongation. Volumetric strain was not recorded during deformation, but matrix porosity of samples measured after deformation remained similar to the starting porosity. Sample deformation is heterogeneous, marked by local necking and formation of grooves parallel to the shear-induced foliation on the sample surfaces (Figures 5a and 5b). The foliation plane is defined by the preferred orientation of the lath-shaped grains that developed with increasing shear strain. These features indicate localization of strain that was previously observed in high-temperature torsion tests on two-phase aggregates of calcite-quartz [*Rybacki et al.*, 2003] and calcite-anhydrite [*Barnhoorn et al.*, 2005].

[19] About 40% of the samples were deformed to final failure at shear strains of < 5. The remaining samples were used to monitor evolution of the microstructure prior to failure. Fracture surfaces are typically helicoidal shaped,

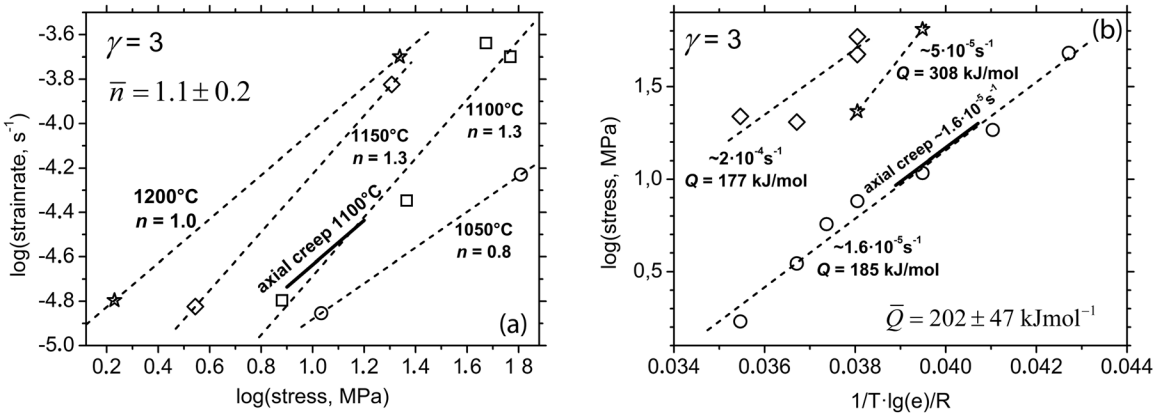

Figure 3. (a) Apparent stress exponent n and (b) activation energy Q for anorthite twisted at different temperatures and strain rates. Stress data are plotted at a shear strain of 3. For comparison, the short solid lines show the results of axial (low strain) compression tests [*Rybacki and Dresen*, 2000], which are in excellent agreement. Error bar is less than symbol size.

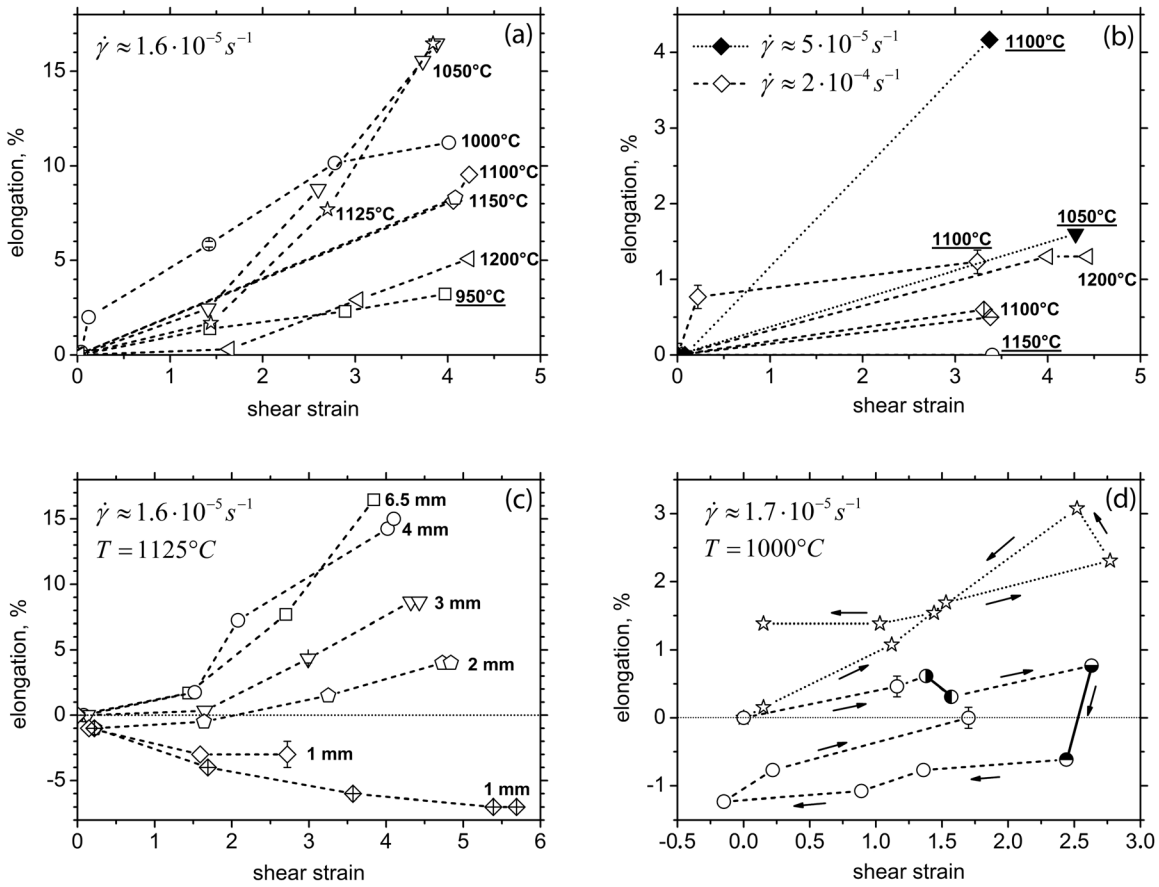

Figure 4. Influence of strain on sample elongation during torsion deformation. The dependence of elongation on (a and b) temperature at various shear strain rates, (c) initial sample length, and (d) twist reversal. Arrows indicate twisting path. A small axial stress of ≤ 1 MPa was applied in two strain intervals indicated by solid lines. Underlined labels denote final failure of sample.

sometimes rupturing also the adjacent ceramic pistons. The orientation β of these macrofractures varies from 5° to 32° with a mean value of 20° ± 11° to the maximum principal stress σ_1 and 25° ± 11° to the shear plane (Figure 5b). One sample (Pl01_b) shows a fracture oriented parallel to σ_1 that formed during a temperature decrease step (Figure 5c). In contrast, thin samples show smaller cracks parallel to the foliation (Figure 5d).

4.5. Microstructure

[20] The mean grain size (3.7 ± 1.2 μm) and estimated average grain aspect ratio (≈2.5) remain relatively similar to the starting microstructure. Samples Pl01 and Pl02 show a slight bimodal grain size distribution where the size of large and serrated grains is about twice the size of small grains. The matrix porosity, measured on SEM micrographs, is about 1%, irrespective of strain, temperature, and strain rate.

[21] In torsion shear strain γ increases linearly from zero at the center of the solid samples toward the periphery. SEM analysis of sections cut midway through the entire sample parallel to their axis shows development of regularly spaced higher-porosity bands at $\gamma > 2$ (Figure 6a). Sections parallel to the sample axis close to the sample periphery ($\gamma \approx 0.94\ \gamma_{max}$) show that these anastomozing bands are inclined by about 10°–20° to the shear plane and 25°–35° to the maximum compressive stress σ_1, respectively (Figure 6b). At similar shear strain, bands appear less frequently in samples deformed at high temperature, probably due to more efficient diffusional mass transfer and accommodation [*Dimanov et al.*, 2007]. The orientation is almost independent of strain revealing continuous rearrangement with progressive deformation. At high strain, pores and cavities form at grain triple junctions and grain boundaries (Figure 6d). Rotation of high-aspect ratio grains within the bands indicates progressive shearing along the bands (Figures 6c and 6e). Outside the bands the strain-induced preferred alignment of the high aspect ratio grains defines a strong foliation. The spherulitic domains initially present in some samples progressively disappear within increasing strain but slightly disturb the regular spacing of porosity bands at lower strain. The formation of a shape-preferred orientation at constant grain shape in combination with the occurrence of cavities suggests cooperative grain boundary sliding [*Zelin and Mukherjee*, 1996]. In our experiments, the shear bands show an orientation and kinematics that are similar to those of C′-type or ECC (extensional crenulation cleavage) shear bands from natural mylonite zones [*Passchier and Trouw*, 1996]. In contrast, short samples with initial length of ≤ 3 mm show almost no shear bands and less cavity damage.

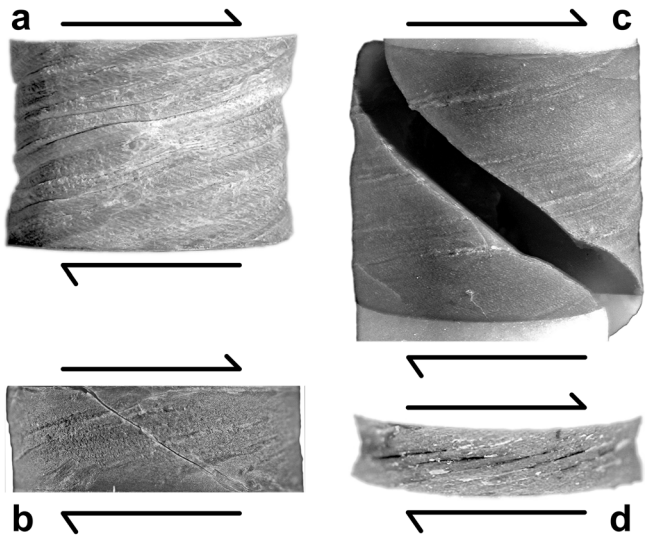

Figure 5. Photographs of twisted anorthite aggregates. (a) Inhomogeneous foliation of an intact sample (Pl10_1). (b) Ductile failure of sample PlT6_4 that formed a macrofrac oriented at an angle β of about 30° to the direction of maximum compressive stress σ_1. (c) Helicoidal shape of a fracture plane that extended into the adjacent alumina pistons (sample Pl_01b). (d) Foliation-parallel mesocracks developed in a deformed short sample (Pl09_4) with an initial length of 2 mm. Shear sense is dextral as indicated by arrows. Deformation conditions are given Table 1.

[22] Since the preparation and thermal etching of SEM sections enhance cavity damage, we inspected ultrathin sections of the shear bands using optical microscopy. SEM observations on thermally etched samples revealed cavities at grain boundaries and grain triple junctions. Ultrathin optical sections and TEM observations show the presence of an amorphous phase in many pores (Figures 6e and 6f). TEM-EDX analysis indicates that the pores are mainly filled with Si-enriched residual glass. In the undeformed samples, the glass (<3 vol%) is homogeneously distributed but not wetting grain boundaries (Figure 7a). In deformed samples, the glass is segregated into the shear bands forming interconnected tubules (Figure 7b). The boundary between the solid and the glass phase is very sharp (Figure 7c) and often enriched in Si. Open pores exist (Figure 7d) but are less frequent.

[23] The mean dislocation density is comparable to that of the starting material. Locally dislocation densities are relatively high (up to 5×10^{13} m^{-2}). Similarly, recrystallized grains form small clusters. Occasionally, subgrains are formed by dislocation arrays (Figures 7d and 7e), which are often limited by twin domains (Figure 7f). Similar to the starting material, fine twins are abundant.

5. Discussion

5.1. Deformation Mechanism

[24] The flow stresses measured in high-strain torsion experiments at constant twist rate are in good agreement with stresses measured in low-strain axial deformation tests at constant strain rate and constant load. The torsion tests allowed to constrain the stress exponent to be $n \approx 1$, indicating that samples deformed by linear-viscous creep (Figures 2 and 3).

[25] The mean activation energy of 202 ± 47 kJ/mol (Figure 3b), estimated from tests covering a temperature range of almost 250°C, is in good agreement with $Q \approx 170 \pm 6$ kJ mol^{-1} determined in axial compression tests on similar material [*Rybacki and Dresen*, 2000; *Rybacki et al.*, 2006]. Temperature steps of 10°C–20°C performed on individual samples yield a significantly higher mean value of 371 ± 76 kJ mol^{-1} and an increase of Q with increasing temperature. This activation energy is close to the value of ≈350 kJ mol^{-1} obtained for dislocation creep of wet fine-grained anorthite aggregates [*Rybacki and Dresen*, 2000; *Rybacki et al.*, 2006]. However, the dislocation density after deformation is similar to the starting material. It remains unclear why Q estimated from temperature stepping is higher than the sample average. It is conceivable that temperature steps induce a transient period of enhanced dislocation activity. Possibly, the high activation energy may be attributed to cavitation since the formation of new surface requires additional energy as suggested by *Nair et al.* [2001]. These authors deformed tabular-shaped anorthite mullite ceramics and found a high creep activation energy and extensive cavitation.

[26] The mechanical data indicate that the fine-grained anorthite aggregates deform by Newtonian-viscous creep ($n \approx 1$). The observed shape-preferred orientation, constant aspect ratio of the grains, and cavitation suggest that grain boundary sliding contributed significantly to deformation. The good agreement between the mechanical data from high-strain torsion tests and low-strain axial compression tests suggests that the dominating deformation mechanisms are similar in both tests. The triaxial deformation experiments revealed grain boundary diffusion-controlled creep [*Rybacki and Dresen*, 2000] with an assumed grain size exponent of $m \sim 3$ that is based on high-temperature creep experiments on synthetic plagioclase aggregates [*Wang et al.*, 1996; *Dimanov et al.*, 1998]. Consequently, we assume that this mechanism controls sample deformation also in torsion tests. Synchrotron X-ray diffraction measurements on some twisted samples [*Gomez Barreiro et al.*, 2007] showed the evolution of a strong texture that may be explained by formation of a shape-preferred orientation, possibly assisted by grain boundary dislocation activity.

[27] It is generally assumed that creep accommodated by diffusion requires grain boundary sliding (GBS) to accommodate high-strain deformation [*Mori et al.*, 1998; *Sahay and Murty*, 2001; *Wang*, 2000]. Models assuming diffusion-assisted GBS generally predict that the strain rate is linearly proportional to the applied stress, whereas models for dislocation-accommodated GBS generally predict a stress exponent n > 1 [*Ashby and Verrall*, 1973; *Chokshi and Langdon*, 1991; *Gifkins*, 1977; *Langdon*, 1970; 2000; *Paterson*, 2001].

5.2. Comparison With Other Studies on Cavitation and Fluid Redistribution in Experimentally Deformed Rocks

[28] The empirical Goetze criterion [*Kohlstedt et al.*, 1995] predicts that crack-induced dilatancy is suppressed when the differential stress is less than the effective confining pressure. *Walker et al.* [1990] observed the formation of voids in HT-HP deformation experiments on fine-grained synthetic calcite

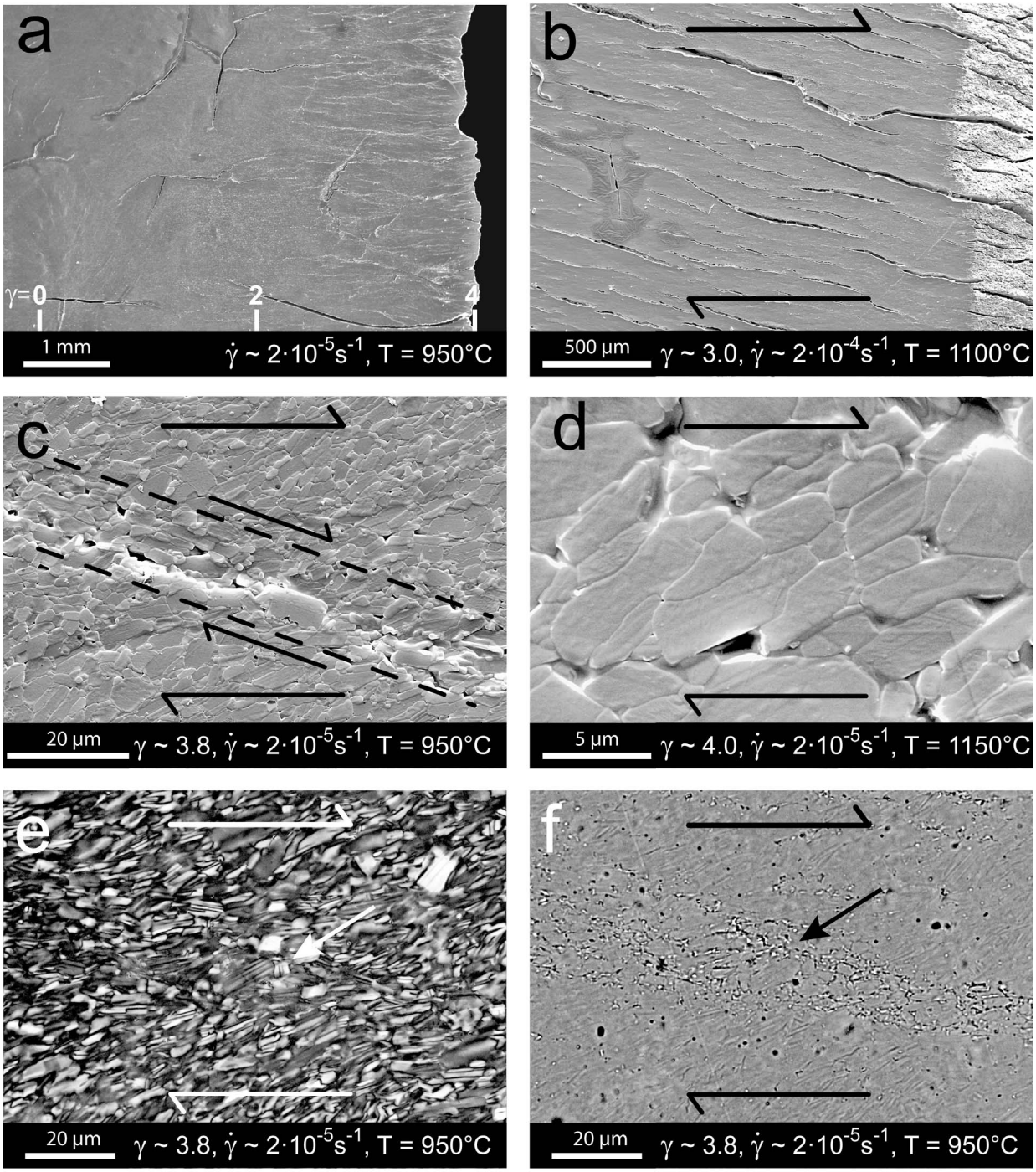

Figure 6. SEM (Figures 6a–6d) and optical (Figures 6e and 6f) micrographs of twisted anorthite samples. (a) Longitudinal-axial section showing the right half of a deformed sample. Cavity damage increases with strain visualized by the onset of strings (whitish lines) at a shear strain above ≈2. Open (dark) cracks result from decompression and cooling of sample. Figures 6b–6f show tangential-longitudinal section close to the sample surface. (b) At high strain anastomozing, regularly spaced cavity strings develop that are oriented about 15° to the shear plane. The appearance of strings is enhanced by thermal etching, polishing, and depressurization after testing. (c) Rotation of grains occurs in narrow synthetic shear bands (indicated by dashed lines), which show abundant cavities that evolve at grain boundaries, and (d) grain triple junctions. Comparison of a shear band (arrow) inspected with (e) crossed nicols and (f) transmitted light shows that the string-forming pore volume contains redistributed residual glass of the starting material (whitish spots in Figure 6f). Scale bars and experimental conditions are labeled at the bottom of each figure. Shear sense is indicated by arrows. Figures 6a, 6c, 6e, and 6f are for sample Pl12_1. Figure 6b is for sample Pl10_3. Figure 6d is for sample Pl10_2.

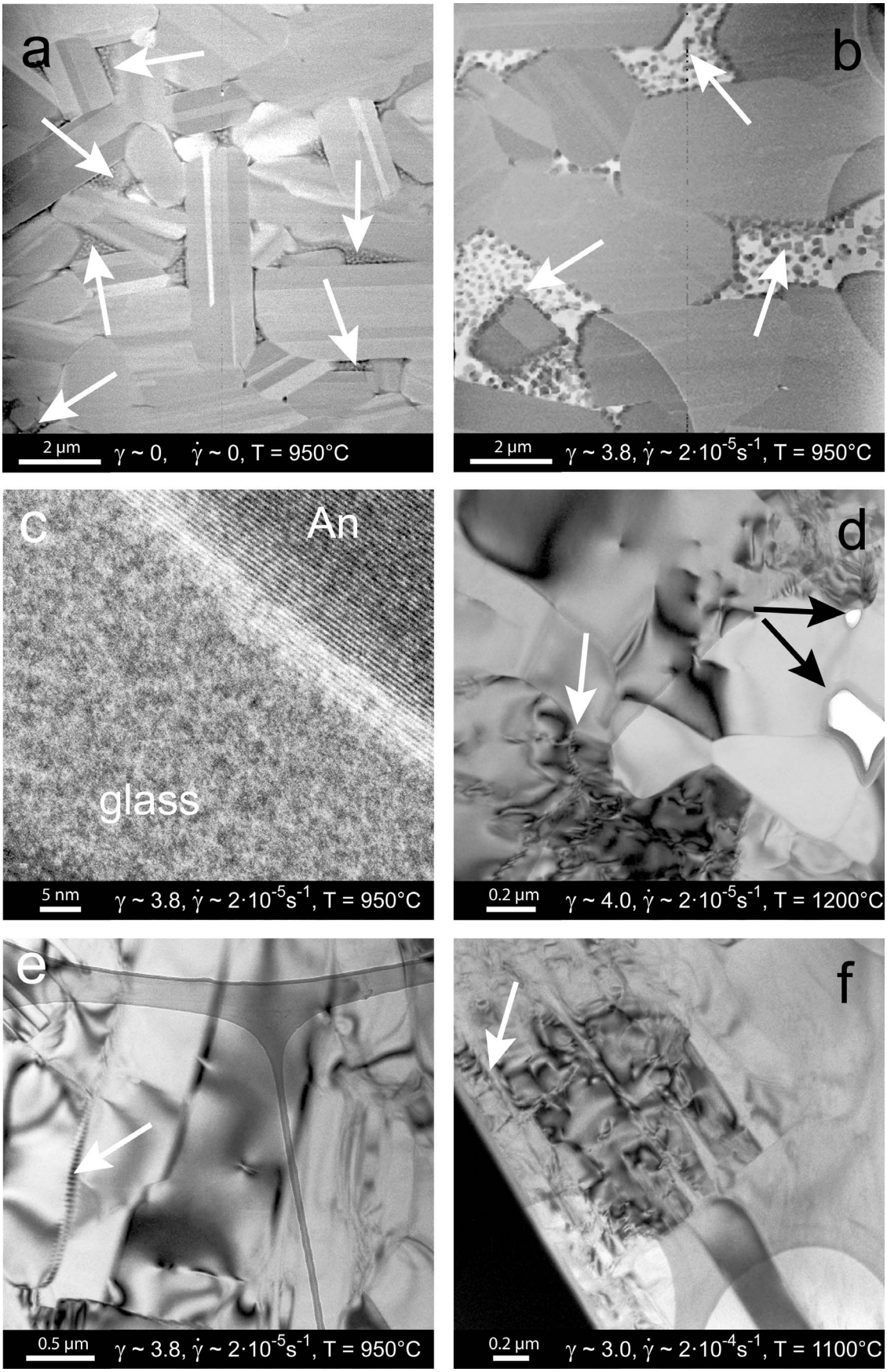
a
2 μm
γ ~ 0, $\dot{\gamma}$ ~ 0, T = 950°C
b
2 μm
γ ~ 3.8, $\dot{\gamma}$ ~ 2·10^{-5}s^{-1}, T = 950°C
c
An
glass
5 nm
γ ~ 3.8, $\dot{\gamma}$ ~ 2·10^{-5}s^{-1}, T = 950°C
d
0.2 μm
γ ~ 4.0, $\dot{\gamma}$ ~ 2·10^{-5}s^{-1}, T = 1200°C
e
0.5 μm
γ ~ 3.8, $\dot{\gamma}$ ~ 2·10^{-5}s^{-1}, T = 950°C
f
0.2 μm
γ ~ 3.0, $\dot{\gamma}$ ~ 2·10^{-4}s^{-1}, T = 1100°C

Figure 7

aggregates at high strain, which they attributed to grain boundary sliding. The measured flow stress was about 5–20 times lower than the confining pressure of ≈200 MPa.

[29] Plagioclase aggregates similar to the material of this study were deformed at high temperature in linear viscous creep and showed no significant cavitation at axial strains up to about 15% shortening at 0.1 and 300 MPa pressure, respectively [*Wang et al.*, 1996; *Dimanov et al.*, 1999; *Rybacki and Dresen*, 2000]. *Nair et al.* [2001] observed strong cavitation in synthetic anorthite aggregates with ≈10% mullite added when deformed at ambient pressure. Cavitation was suppressed at elevated pressures of 300 MPa. The authors also found that cavitation was more pronounced for aggregates with elongated grains compared to equiaxed grains. Fine-grained anorthite-diopside aggregates with less than 1 vol% residual glass deformed in torsion at low stresses and a confining pressure of 400 MPa showed cavitation and their coalescence leading to sample failure [*Dimanov et al.*, 2007]. Open voids and cavities formed preferentially at interphase and diopside-diopside boundaries. TEM observations suggest that grain boundary sliding was associated with dislocation activity. The results suggest that cavitation is enhanced in the presence of a second phase [*Dimanov et al.*, 2007].

[30] Redistribution of aqueous fluids from isolated pores to grain boundaries was observed in triaxial compression experiments at 1.4 GPa confining pressure on water-added, fine-grained albite aggregates that deformed by fluid-assisted grain boundary diffusion creep and grain boundary sliding [*Tullis et al.*, 1996]. Flow stress was estimated to be less than 25 MPa. Torsion experiments on fine-grained wet Dover flint [*Schmocker et al.*, 2003] showed evidence for granular flow at shear stresses of about 1/3 to 1/2 of the confinement (350 MPa). The authors suggested that deformation was accommodated by diffusive mass transfer through the liquid. At high strain a redistribution of pores along anastomozing shear bands occurred. The bands were oriented about ± 25° to the maximum principal stress direction. Previously, *Holtzman et al.* [2003a, 2003b] and *Kohlstedt et al.* [2009] observed melt migration into shear bands in deformation experiments on synthetic olivine and anorthite aggregates containing < 12% melt of MORB composition. The bands were oriented about 15°–20° to the shear plane and ~25°–30° to the maximum principal stress and formed at shear stresses between 50 and 150 MPa at 300 MPa confining pressure. The authors suggest that melt segregation was driven by a fluid pressure gradient. The low-viscosity melt assisted in relaxation of local stress concentrations, thus suppressing cavitation [*Hier-Majumder et al.*, 2004; *Kohlstedt et al.*, 2009]. In contrast, we estimate the viscosity of the residual glass in our samples to be about 3 orders (for anorthitic melt) to 10 orders (for Si-enriched melt) of magnitude higher than MORB at experimental conditions [*Hui and Zhang*, 2007].

[31] Our experiments indicate that cavitation evolves during high-temperature creep of geologic materials at flow stresses that are significantly smaller than the effective confining pressure. This is in striking contrast to observations on metals and alloys. For these materials, application of a hydrostatic pressure on the order of the flow stress is found to effectively suppress cavitation [*Bampton and Raj*, 1982; *Pilling and Ridley*, 1988; *Zaki*, 1998; *Nicolaou and Semiatin*, 2003]. Grain boundary sliding likely contributes more significantly to strain accommodation in rocks as more slip systems are available in metals and alloys. In addition, the presence of a pore fluid, second phases, or high-aspect ratio grains may prevent closure of newly created pores.

5.3. Sample Hardening and Elongation

[32] Samples deformed at slow strain rate ($\approx 10^{-5}$ s^{-1}) show continuous hardening and elongation with increasing strain. The hardening rate decreases above $\gamma \approx 1$ by 1 order of magnitude with temperature increasing from 950°C to 1200°C. At constant torque, shear stress increases with decreasing sample diameter cubed. Assuming constant sample volume, about 5–15% of the hardening may be attributed to sample elongation and associated reduction of the sample diameter.

[33] Although we were not able to record change of porosity during deformation, measurements on deformed samples indicate a total porosity of < 3%. Also, the matrix porosity measured on some SEM sections in between cavity bands remains at about 1% after testing. The resistance to deformation can be expressed as $\tau_w = \tau - P \cdot (d\varphi/d\gamma)$, where P is the effective confining pressure and $d\varphi$ is change in porosity per increment in shear strain $d\gamma$ [*Edmond and Paterson*, 1972; *Fischer and Paterson*, 1989]. A porosity increase between ≈30% at 950°C and ≈1% at 1200°C would be required to fully account for the measured hardening at 10^{-5} s^{-1} strain rate. This rules out that the observed hardening is related to cavitation-induced dilatancy, at least at low temperatures.

[34] Grain growth during deformation will result in a strengthening of the aggregates. The average grain size of deformed specimens remains similar to the starting material, but the statistical error is about 30%. An increase in grain size between 40% and 60% would be required to account for the hardening observed at slow strain rates, assuming a grain size sensitivity of m = 2–3 [*Gifkins*, 1977; *Dimanov et al.*, 1999; *Wang*, 2000]. This suggests that only a fraction of the observed hardening may be due to grain growth. Reversal of the shear sense during the tests results in a significantly

Figure 7. TEM micrographs of undeformed and deformed feldspar samples. (a) Si-enriched residual glass (white arrows) of the starting material that is homogeneously distributed at three and four grain junctions in undeformed and low strain regions (b) rearranged in interconnected channels along the cavity strings in the highly strained shear bands. Dark glass area is nearly pure Si, and white parts contain additionally Fe and Mn. (c) The interface between glass and An crystal is usually sharp and enriched in Si (bright band). (d) Intergranular small open pores (black arrows) are also present at high strain. (e) Subgrains decorated by dislocation arrays (white arrows) are created in some regions of relatively high dislocation density (also Figure 7d). (f) Dislocations are often bound by twin domains. Scale bars and experimental conditions are labeled at the bottom of each figure. Figures 7a, 7b, 7c, and 7e are for sample Pl12_1. Figure 7d is for sample Pl11_1. Figure 7f is for sample Pl10_3.

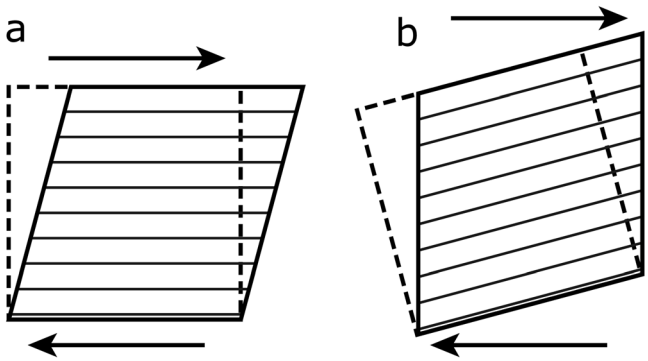

Figure 8. Shearing of a volume element (dashed lines) with shear planes (a) parallel and (b) inclined to the shear direction, indicated by arrows. Sample elongation will occur in orientation of Figure 8b. Shear planes may represent slip planes or grain boundaries.

enhanced hardening rate (Figure 1e). This cannot be explained exclusively by grain growth.

[35] The samples develop a shape-preferred orientation of the high aspect ratio of feldspar grains resulting in a pronounced foliation. The long axis of the grains is oriented at 10°–35° to the shear plane (Figure 6). A component of grain boundary sliding along the foliation direction will result in sample elongation. The mechanism is reminiscent of the Swift effect found in metals deformed to high strain [*Swift*, 1947]. The Swift effect relates a change in axial dimension during torsion to the orientation of dislocation glide planes with respect to the macroscopic shear plane. For crystals with slip planes oriented parallel to the shear direction sample length is expected to remain constant. However, a finite elongation/shortening may develop if slip is preferably activated on glide planes inclined to the shear direction (Figure 8). The Swift effect was also observed in high-temperature torsion experiments on calcite rocks [*Rybacki et al.*, 2003] and metal alloys [*Klöden et al.*, 2007], where dislocation creep was dominant. It is conceivable that preferential sliding along grain boundaries subparallel to the foliation may impose kinematic constraints similar to those of the Swift effect. This is supported by the observation that previously elongated samples shorten when the shear sense is reversed (Figure 4d).

[36] An intriguing observation is that hardening and sample elongation are only observed at lower strain rates. Samples deformed at higher strain rates and high stress show slight weakening and almost no elongation (Figure 1c), which is likely linked to the increased density of porosity bands observed at lower temperature (higher stress). Shearing along these conjugate bands may compensate for the foliation-related elongation and also reduce strain hardening by localized stress relaxation.

5.4. Cavitation and Ductile Failure

[37] Ductile failure is commonly observed in high-strain tensile testing of metals and ceramics at ambient pressure. Depending on temperature and stress/strain rate, fracture modes may be distinguished into (1) cleavage fracture, i.e., breaking of atomic bonds; (2) void growth and coalescence by plastic flow, often resulting in transgranular fracture; (3) cavity growth and coalescence by diffusive and/or plastic processes resulting in intergranular creep fracture; and (4) stress corrosion cracking under certain chemical environments [*Ashby et al.*, 1979; *Gandhi and Ashby*, 1979; *Riedel*, 1986]. In tension, dynamic recrystallization may also result in rupture.

[38] Reviews of high-temperature creep damage mechanisms are given by *Kassner and Hayes* [2003], *Riedel* [1986, 1993], and *Stowell* [1983]. The theoretical approaches involve nucleation of cavities and voids or wedges and subsequent growth, either of them possibly rate controlling [*Kassner and Hayes*, 2003; *Riedel*, 1986, 1993; *Tvergaard*, 1990; 2009]. Mechanisms of cavity nucleation are still poorly understood. Nucleation may occur in response to grain boundary sliding, accumulation of vacancies, or due to the pileup of dislocations. Preferred nucleation sites are triple points and grain boundary ledges and high-stress regions along grain boundaries. Second-phase particles and pores are also potential nucleation sites (Figure 9). Cavity growth may be controlled by grain boundary sliding, dislocation activity, grain boundary and surface diffusion or any combination of these. In our experiments, we did not observe appreciable acceleration or weakening before failure finally occurred. In our samples, formation and coalescence of cavities and voids are associated with a redistribution of porosity and minor amounts of residual melt. A significant change in total porosity could not be measured. Finally, linkage of cavities and fissures leads to intergranular creep fracture where the trace of the macroscopic fracture plane is oriented by about $20° \pm 11°$ to σ_1. Ductile failure of feldspar aggregates is likely controlled by a critical total strain [*Rybacki et al.*, 2008]. Cavitation-induced failure in high-strain torsion experiments was also observed in anorthite-diopside aggregates [*Dimanov et al.*, 2007] and calcite-muscovite aggregates [*Delle Piane et al.*, 2009].

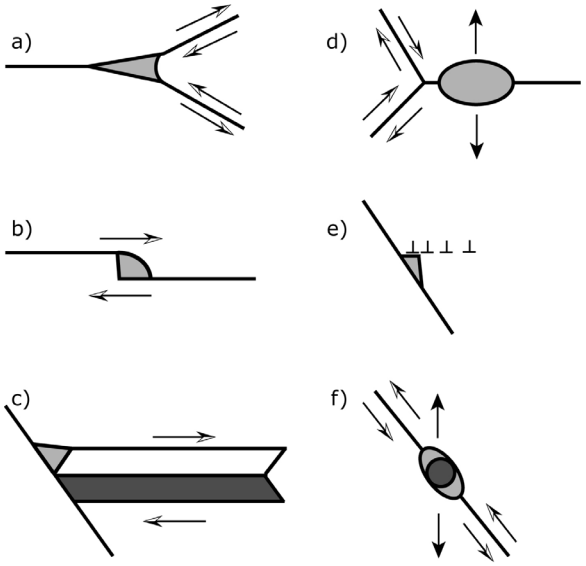

Figure 9. Cavity nucleation mechanisms: (a) wedging at grain triple points, (b) grain boundary ledges, (c) twinning, (d) vacancy condensation at high stress regions, (e) dislocation pileup, (f) particle obstacles (modified from the works of *Riedel* [1986] and *Kassner and Hayes* [2003]).

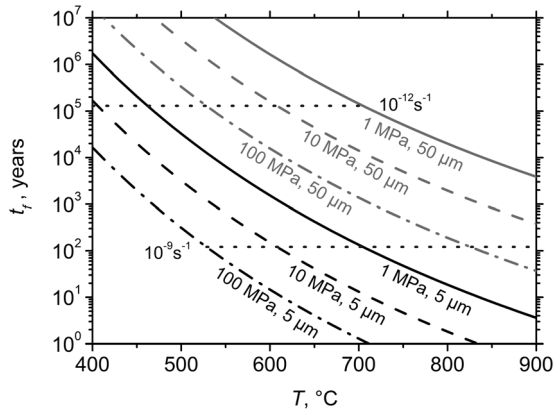

Figure 10. Prediction of ductile failure time t_f versus temperature based on the Monkman-Grant relation and the flow law parameters for grain boundary diffusion controlled creep of wet anorthite [*Rybacki and Dresen*, 2000]. Contours are plotted for constant flow stress (in MPa) and grain size (in μm). Dotted horizontal lines show failure times for labeled steady state shear strain rates.

5.5. Geological Application

[39] Diffusion-assisted grain boundary sliding was frequently suggested to occur in feldspar rocks based on microstructure analysis of ultramylonites spanning a temperature range from 250°C to 700°C [*Kerrich et al.*, 1980; *Molli*, 1994; *Fliervoet et al.*, 1997; *Kenkmann and Dresen*, 2002; *Rosenberg and Stünitz*, 2003; *Zavada et al.*, 2007]. The occurrence of cavities at grain boundaries and triple junctions and high porosity was reported for natural quartz and feldspar-bearing ultramylonites [*White and White*, 1983; *Behrmann*, 1985; *Behrmann and Mainprice*, 1987; *Mancktelow et al.*, 1998; *Zavada et al.*, 2007]. *Geraud et al.* [1995] measured up to 8% porosity in the high-strain cores of a granitic shear zone. The authors estimated that permeability of the shear zone was increased by an order of magnitude in comparison to the wall rock. Therefore, enhanced fluid flow in high-temperature shear zones [*Rutter and Brodie*, 1985; *Fusseis et al.*, 2009] and CO_2 degassing of the uppermost mantle [*Regenauer-Lieb*, 1998] may be attributed to cavitation damage.

[40] *Shigematsu et al.* [2004, 2009] reported abundant microvoids and brittle fractures in a greenschist facies mylonite zone at temperatures of about 340°C. The nucleation of earthquakes at the base of the seismogenic zone was suggested to be related to cavitation and ductile fracturing [*Shigematsu et al.*, 2009]. Coexistence of pseudotachylyte melts and ultramylonites below the seismogenic zone may suggest that plastic instabilities may trigger seismic events [*Hobbs et al.*, 1986; *White*, 1996]. We suggest that ductile failure of ultramylonite zones may provide a viable mechanism inducing earthquakes in the lower crust [*Maggi et al.*, 2000]. Likewise, ductile failure is a possible mechanism explaining the occurrence of intermediate and deep nonvolcanic tremors in subduction zones [*Obara*, 2002; *Obara and Hirose*, 2006; *Ito and Obara*, 2006; *Ito et al.*, 2007; *Brown et al.*, 2009] and fault zones [*Nadeau and Dolenc*, 2005], which are commonly assumed to be generated by dehydration reactions and/or fluid pressure pulses.

[41] The ductile failure of superplastic metals in uniaxial tension at constant stress is empirically described by the Monkman-Grant relationship

$$\dot{\gamma}^k \times t_f = C, \tag{2}$$

where $\dot{\gamma}$ is the steady state creep rate, t_f is the time to failure, and k and C are constants [*Dunand et al.*, 1999; *Kassner and Hayes*, 2003; *Phaniraj et al.*, 2003]. This relationship was frequently verified for metals and alloys with an exponent k close to unity. We applied equation (2) onto our high-temperature torsion data of anorthite, although obtained at constant twist rates at different temperatures and stresses. The result yields the constants $k = 1.01 \pm 0.08$ and $C = 3.1 \pm 2.5$, respectively, which is quite similar to estimates based on experiments performed solely at 400 MPa confining pressure [*Rybacki et al.*, 2008]. Combining equations (1) and (2) allows speculating on the time to failure under geological strain rates. Figure 10 shows t_f contours versus temperature for shear stresses of 1, 10, and 100 MPa and two different grain sizes of 5 and 50 μm, respectively, using the power law parameters for grain boundary diffusion-controlled creep of wet anorthite aggregates determined by *Rybacki and Dresen* [2000]. At given stress, t_f is reduced by about 3 orders of magnitude if grain size is decreased by a factor of 10 due to associated increased shear strain rate. Alternatively, at given grain size t_f is reduced by ≈2 orders of magnitude if the stress is decreased by 2 orders of magnitude that is related to the magnitude of the constant k. The estimated time to failure varies between ≈120 and ≈130,000 years for estimated strain rates for natural shear zones of 10^{-9} to 10^{-12} s^{-1}, respectively, corresponding to a shear strain to failure of about 3.9. On the basis of the predicted relatively short time interval for ductile failure of anorthite in a fast creeping shear zone, we infer that recently discovered seismic phenomena in high-strain fault and subduction zones, such as low-frequency earthquakes, slow slip events, and tremor, may result from episodic failure of lower crustal rocks associated with pore fluid redistribution [*Thomas et al.*, 2009].

[42] **Acknowledgments.** We thank M. Naumann for running the torsion tests and S. Gehrmann, K. Peach, and A. Schreiber for thin section and FIB-foil preparation. A. Dimanov and an anonymous reviewer provided very helpful reviews.

References

Ashby, M., and M. Verrall (1973), Diffusion-accommodated flow and superplasticity, *Acta Metall.*, *21*, 149–163, doi:10.1016/0001-6160(73)90057-6.

Ashby, M., C. Gandhi, and D. Taplin (1979), Fracture-mechanism maps and their construction for F.C.C. metals and alloys, *Acta Metall.*, *27*, 699–729, doi:10.1016/0001-6160(79)90105-6.

Austrheim, H., and T. M. Boundy (1994), Pseudotachylytes generated during seismic faulting and eclogitization of the deep crust, *Science*, *265*, 82–83, doi:10.1126/science.265.5168.82.

Bampton, C. C., and R. Raj (1982), Influence of hydrostatic pressure and multiaxial straining on cavitation in a superplastic aluminum alloy, *Acta Mater.*, *30*, 2043–2053, doi:10.1016/0001-6160(82)90107-9.

Barnhoorn, A., M. Bystricky, K. Kunze, L. Burlini, and J.-P. Burg (2005), Strain localisation in bimineralic rocks: Experimental deformation of synthetic calcite-anhydrite aggregates, *Earth Planet. Sci. Lett.*, *240*(3–4), 748–763, doi:10.1016/j.epsl.2005.09.014.

Behrmann, J. H. (1985), Crystal plasticity and superplasticity in quartzite; A natural example, *Tectonophysics*, *115*(1–2), 101–129, doi:10.1016/0040-1951(85)90102-7.

Behrmann, J. H., and D. Mainprice (1987), Deformation mechanisms in a high-temperature quartz-feldspar mylonite: Evidence for superplastic

flow in the lower continental crust, *Tectonophysics*, *140*, 297–305, doi:10.1016/0040-1951(87)90236-8.

Brown, J. R., G. C. Beroza, S. Ide, K. Ohta, D. R. Shelly, S. Y. Schwartz, W. Rabbel, M. Thorwart, and H. Kao (2009), Deep low-frequency earthquakes in tremor localize to the plate interface in multiple subduction zones, *Geophys. Res. Lett.*, *36*, L19306, doi:10.1029/2009GL040027.

Chokshi, A. H., and T. G. Langdon (1991), Overview: Characteristics of creep deformation in ceramics, *Mater. Sci. Technol.*, *7*, 577–584.

Delle Piane, C., C. J. L. Wilson, and L. Burlini (2009), Dilatant plasticity in high-strain experiments on calcite-muscovite aggregates, *J. Struct. Geol.*, *31*(10), 1084–1099, doi:10.1016/j.jsg.2009.03.005.

Dimanov, A., G. Dresen, and R. Wirth (1998), High-temperature creep of partially molten plagioclase aggregates, *J. Geophys. Res.*, *103*, 9651–9664, doi:10.1029/97JB03742.

Dimanov, A., G. Dresen, X. Xiao, and R. Wirth (1999), Grain boundary diffusion creep of synthetic anorthite aggregates: The effect of water, *J. Geophys. Res.*, *104*, 10,483–10,497, doi:10.1029/1998JB900113.

Dimanov, A., E. Rybacki, R. Wirth, and G. Dresen (2007), Creep and strain-dependent microstructures of synthetic anorthite-diopside aggregates, *J. Struct. Geol.*, *29*(6), 1049–1069, doi:10.1016/j.jsg.2007.02.010.

Dunand, D. C., B. Q. Han, and A. M. Jansen (1999), Monkman-Grant analysis of creep fracture in dispersion-strengthened and particulate-reinforced aluminium, *Metall. Mater. Trans. A*, *30*(13), 829–838, doi:10.1007/s11661-999-1016-6.

Edmond, J., and M. Paterson (1972), Volume changes during the deformation of rocks at high pressures, *Int. J. Rock Mech. Min. Sci.*, *9*, 161–182, doi:10.1016/0148-9062(72)90019-8.

Fischer, G., and M. Paterson (1989), Dilatancy during rock deformation at high temperatures and pressures, *J. Geophys. Res.*, *94*, 17,607–17,617, doi:10.1029/JB094iB12p17607.

Fliervoet, T. F., S. H. White, and M. R. Drury (1997), Evidence for dominant grain-boundary sliding deformation in greenschist- and amphibolite-grade polymineralic ultramylonites from the Redbank Deformed Zone, Central Australia, *J. Struct. Geol.*, *19*, 1495–1520, doi:10.1016/S0191-8141(97)00076-X.

Fusseis, F., K. Regenauer-Lieb, J. Liu, R. M. Hough, and F. De Carlo (2009), Creep cavitation can establish a dynamic granular fluid pump in ductile shear zones, *Nature*, *459*(7249), 974–977, doi:10.1038/nature08051.

Gandhi, C., and M. Ashby (1979), Fracture-mechanism maps for materials which cleave: F.C.C., B.C.C. and H.C.P. metals and ceramics, *Acta Metall.*, *27*, 1565–1602, doi:10.1016/0001-6160(79)90042-7.

Geraud, Y., J.-M. Caron, and P. Faure (1995), Porosity network of a ductile shear zone, *J. Struct. Geol.*, *17*(12), 1757–1769, doi:10.1016/0191-8141(95)00067-N.

Gifkins, R. C. (1977), The effect of grain size and stress upon grain-boundary sliding, *Metall. Trans. A*, *8*, 1507–1516.

Gomez Barreiro, J., I. Lonardelli, H. R. Wenk, G. Dresen, E. Rybacki, Y. Ren, and C. N. Tome (2007), Preferred orientation of anorthite deformed experimentally in Newtonian creep, *Earth Planet. Sci. Lett.*, *264*(1–2), 188–207, doi:10.1016/j.epsl.2007.09.018.

Hier-Majumder, S., P. H. Leo, and D. L. Kohlstedt (2004), On grain boundary wetting during deformation, *Acta Mater.*, *52*(12), 3425–3433, doi:10.1016/j.actamat.2004.03.040.

Hobbs, B., and A. Ord (1988), Plastic instabilities: Implications for the origin of intermediate and deep focus earthquakes, *J. Geophys. Res.*, *93*(B9), 10,521–10,540, doi:10.1029/JB093iB09p10521.

Hobbs, B., A. Ord, and C. Teyssier (1986), Earthquakes in the ductile regime?, *Pure Appl. Geophys.*, *124*, 309–336, doi:10.1007/BF00875730.

Holtzman, B. K., N. J. Groebner, M. E. Zimmerman, S. B. Ginsberg, and D. L. Kohlstedt (2003a), Stress-driven melt segregation in partially molten rocks, *Geochem. Geophys. Geosyst.*, *4*(5), 8607, doi:10.1029/2001GC000258.

Holtzman, B. K., D. L. Kohlstedt, M. E. Zimmerman, F. Heidelbach, T. Hiraga, and J. Hustoft (2003b), Melt segregation and strain partitioning: Implications for seismic anisotropy and mantle flow, *Science*, *301*(5637), 1227–1230, doi:10.1126/science.1087132.

Huenges, E., J. Erzinger, and J. Kück (1997), The permeable crust: Geohydraulic properties down to 9101 m depth, *J. Geophys. Res.*, *102*(B8), 18,255–18,265, doi:10.1029/96JB03442.

Hui, H., and Y. Zhang (2007), Toward a general viscosity equation for natural anhydrous and hydrous silicate melts, *Acta Geochim. Cosmochim.*, *71*(2), 403–416, doi:10.1016/j.gca.2006.09.003.

Ito, Y., and K. Obara (2006), Very low frequency earthquakes within accretionary prisms are very low stress-drop earthquakes, *Geophys. Res. Lett.*, *33*, L09302, doi:10.1029/2006GL025883.

Ito, Y., K. Obara, K. Shiomi, S. Sekine, and H. Hirose (2007), Slow earthquakes coincident with episodic tremors and slow slip events, *Science*, *315*(5811), 503–506, doi:10.1126/science.1134454.

Kassner, M. E., and T. A. Hayes (2003), Creep cavitation in metals, *Int. J. Plast.*, *19*(10), 1715–1748, doi:10.1016/S0749-6419(02)00111-0.

Kenkmann, T., and G. Dresen (2002), Dislocation microstructures and phase distribution in a lower crustal shear zone—An example from the Ivrea-Zone, Italy, *Int. J. Earth Sci.*, *91*, 445–458, doi:10.1007/s00531-001-0236-9.

Kerrich, R., I. Allison, R. L. Barnett, S. Moss, and J. Starkey (1980), Microstructural and chemical transformations accompanying deformation of granite in a shear zone at Mieville, Switzerland; with implications for stress corrosion cracking and superplastic flow, *Contrib. Mineral. Petrol.*, *73*, 221–242, doi:10.1007/BF00381442.

Klöden, B., E. Rybacki, C. G. Oertel, and W. Skrotzki (2007), Grain refinement and texture formation in torsion deformed NiAl, *Int. J. Mater. Res.*, *98*(4), 276–282.

Kohlstedt, D. L., B. Evans, and S. J. Mackwell (1995), Strength of the lithosphere: Constraints imposed by laboratory experiments, *J. Geophys. Res.*, *100*(B9), 17,587–17,602, doi:10.1029/95JB01460.

Kohlstedt, D. L., M. E. Zimmerman, and S. J. Mackwell (2009), Stress-driven melt segregation in partially molten feldspathic rocks, *J. Petrol.*, doi:10.1093/petrology/egp1043.

Landuyt, W., and D. Bercovici (2009), Formation and structure of lithospheric shear zones with damage, *Phys. Earth Planet. Inter.*, *175*(3–4), 115–126, doi:10.1016/j.pepi.2009.03.005.

Langdon, T. G. (1970), Grain boundary sliding as a deformation mechanism during creep, *Philos. Mag.*, *22*, 689–700, doi:10.1080/14786437008220939.

Langdon, T. G. (2000), Identifying creep mechanisms at low stresses, *Mater. Sci. Eng. A*, *283*(1–2), 266–273, doi:10.1016/S0921-5093(00)00624-9.

Maggi, A., J. A. Jackson, D. McKenzie, and K. Priestley (2000), Earthquake focal depth, effective elastic thickness, and the strength of the continental lithosphere, *Geology*, *28*(6), 495–498, doi:10.1130/0091-7613(2000)28<495:EFDEET>2.0.CO;2.

Mancktelow, N. S., D. Grujic, and E. L. Johnson (1998), An SEM study of porosity and grain boundary microstructure in quartz mylonites, Simplon fault zone, Central Alps, *Contrib. Mineral. Petrol.*, *131*, 71–85, doi:10.1007/s004100050379.

Molli, G. (1994), Microstructural features of high temperature shear zones in gabbros of the Northern Apennine Ophiolites, *J. Struct. Geol.*, *16*(11), 1535–1541, doi:10.1016/0191-8141(94)90031-0.

Mori, T., S. Onaka, and K. Wakashima (1998), Role of grain-boundary sliding in diffusional creep of polycrystals, *J. Appl. Phys.*, *83*(12), 7547–7552, doi:10.1063/1.367519.

Nadeau, R. M., and D. Dolenc (2005), Nonvolcanic tremors deep beneath the San Andreas Fault, *Science*, *307*(5708), 389, doi:10.1126/science.1107142.

Nair, B. G., R. F. Cooper, D. Bruhn, and D. L. Kohlstedt (2001), High-temperature rheology of calcium aluminosilicate (anorthite) glass-ceramics under uniaxial and triaxial loading, *J. Am. Ceram. Soc.*, *84*(11), 2617–2624, doi:10.1111/j.1151-2916.2001.tb01062.x.

Nicolaou, P. D., and S. L. Semiatin (2003), An experimental and theoretical investigation of the influence of stress state on cavitation during hot working, *Acta Mater.*, *51*(3), 613–623, doi:10.1016/S1359-6454(02)00441-X.

Obara, K. (2002), Nonvolcanic deep tremor associated with subduction in southwest Japan, *Science*, *296*(5573), 1679–1681, doi:10.1126/science.1070378.

Obara, K., and H. Hirose (2006), Non-volcanic deep low-frequency tremors accompanying slow slips in the southwest Japan subduction zone, *Tectonophysics*, *417*(1–2), 33–51, doi:10.1016/j.tecto.2005.04.013.

Passchier, C. W., and R. A. J. Trouw (1996), *Microtectonics*, 289 pp., Springer, Berlin.

Paterson, M. S. (1990), Superplasticity in geological materials, *Mat. Res. Soc. Symp. Proc.*, *196*, 303–312.

Paterson, M. S. (2001), A granular flow theory for the deformation of partially molten rock, *Tectonophysics*, *335*, 51–61, doi:10.1016/S0040-1951(01)00045-2.

Paterson, M. S., and D. L. Olgaard (2000), Rock deformation tests to large shear strains in torsion, *J. Struct. Geol.*, *22*, 1341–1358, doi:10.1016/S0191-8141(00)00042-0.

Paterson, M. S., and T. F. Wong (2005), *Experimental Rock Deformation—The Brittle Field*, 2nd ed., 347 pp., Springer, Berlin.

Phaniraj, C., B. K. Choudhary, K. Bhanu Sankara Rao, and B. Raj (2003), Relationship between time to reach Monkman-Grant ductility and rupture life, *Scr. Mater.*, *48*(9), 1313–1318, doi:10.1016/S1359-6462(03)00021-6.

Pilling, J., and N. Ridley (1988), Cavitation in superplastic alloys and the effect of hydrostatic pressure, *Res. Mech.*, *23*, 31–63.

Regenauer-Lieb, K. (1998), Dilatant plasticity applied to Alpine collision: Ductile void growth in the intraplate area beneath the Eifel volcanic field, *J. Geodyn.*, *27*(1), 1–21, doi:10.1016/S0264-3707(97)00024-0.

Renshaw, C. E., and E. M. Schulson (2004), Plastic faulting: Brittle-like failure under high confinement, *J. Geophys. Res.*, *109*, B09207, doi:10.1029/2003JB002945.

Riedel, H. (1986), *Fracture at High Temperature*, 423 pp., Springer, Berlin.

Riedel, H. (1993), Fracture mechanics, in *Plastic Deformation and Fracture of Materials*, edited by H. Mughrabi, pp. 565–628, VCH, Weinheim, Germany.

Rosenberg, C. L., and H. Stünitz (2003), Deformation and recrystallization of plagioclase along a temperature gradient: An example from the Bergell tonalite, *J. Struct. Geol.*, *25*, 389–408, doi:10.1016/S0191-8141(02)00036-6.

Rutter, E. H., and K. H. Brodie (1985), The permeation of water into hydrating shear zones, in *Metamorphic Reactions, Kinetics, Textures, and Deformation*, edited by A. B. Thompson and D. C. Rubie, pp. 242–250, Springer, New York.

Rybacki, E., and G. Dresen (2000), Dislocation and diffusion creep of synthetic anorthite aggregates, *J. Geophys. Res.*, *105*(B11), 26,017–26,036, doi:10.1029/2000JB900223.

Rybacki, E., M. S. Paterson, R. Wirth, and G. Dresen (2003), Rheology of calcite-quartz aggregates deformed to large strain in torsion, *J. Geophys. Res.*, *108*(B2), 2089, doi:10.1029/2002JB001833.

Rybacki, E., M. Gottschalk, R. Wirth, and G. Dresen (2006), Influence of water fugacity and activation volume on the flow properties of fine-grained anorthite aggregates, *J. Geophys. Res.*, *111*, B03203, doi:10.1029/2005JB003663.

Rybacki, E., R. Wirth, and G. Dresen (2008), High-strain creep of feldspar rocks: Implications for cavitation and ductile failure in the lower crust, *Geophys. Res. Lett.*, *35*, L04304, doi:10.1029/2007GL032478.

Sahay, S. S., and G. S. Murty (2001), Uncertainty in separating the strain contributions of sliding and diffusion in diffusional creep, *Scr. Mater.*, *44*, 841–845, doi:10.1016/S1359-6462(00)00655-2.

Schmocker, M., M. Bystricky, K. Kunze, and L. Burlini (2003), Granular flow and Riedel band formation in water-rich quartz aggregates experimentally deformed in torsion, *J. Geophys. Res.*, *108*(B5), 2242, doi:10.1029/2002JB001958.

Shigematsu, N., K. Fujimoto, T. Ohtani, and K. Goto (2004), Ductile fracture of fine-grained plagioclase in the brittle-plastic transition regime: Implication for earthquake source nucleation, *Earth Planet. Sci. Lett.*, *222*(3–4), 1007–1022, doi:10.1016/j.epsl.2004.04.001.

Shigematsu, N., K. Fujimoto, T. Ohtani, B. Shibazaki, T. Tomita, H. Tanaka, and Y. Miyashita (2009), Localisation of plastic flow in the mid-crust along a crustal-scale fault: Insight from the Hatagawa Fault Zone, NE Japan, *J. Struct. Geol.*, *31*(6), 601–614, doi:10.1016/j.jsg.2009.04.004.

Stowell, M. J. (1983), Failure of superplastic alloys, *Metal Sci.*, *17*, 1–11.

Swift, R. W. (1947), Length changes in metals under torsional overstrain, *Engineering*, *164*, 253–257.

Thomas, A. M., R. M. Nadeau, and R. Bürgmann (2009), Tremor-tide correlations and near-lithostatic pore pressure on the deep San Andreas fault, *Nature*, *462*, 1048–1051, doi:10.1038/nature08654.

Tullis, J., and R. A. Yund (1991), Diffusion creep in feldspar aggregates: Experimental evidence, *J. Struct. Geol.*, *13*, 987–1000, doi:10.1016/0191-8141(91)90051-J.

Tullis, J., R. Yund, and J. Farver (1996), Deformation-enhanced fluid distribution in feldspar aggregates and implications for ductile shear zones, *Geology*, *24*, 63–66, doi:10.1130/0091-7613(1996)024<0063:DEFDIF>2.3.CO;2.

Tvergaard, V. (1990), Material failure by void growth to coalescence, in *Advances in Apllied Mechanics*, edited by J. W. Hutchinson and T. Y. Wu, pp. 83–151, Elsevier, New York.

Tvergaard, V. (2009), Behaviour of voids in a shear field, *Int. J. Fract.*, *158*(1), 41–49, doi:10.1007/s10704-009-9364-1.

Underwood, E. E. (1970), *Quantitative Stereology*, 274 pp., Addison Wesley, Boston, Mass.

Walker, A., E. Rutter, and K. Brodie (1990), Experimental study of grain-size sensitive flow of synthetic, hot-pressed calcite rocks, in *Deformation, Mechanisms, Rheology and Tectonics*, edited by R. J. Knipe and E. H. Rutter, *Geol. Soc. Spec. Publ.*, *200*, 259–284.

Wang, J. N. (2000), An investigation of the deformation mechanism in grain size-sensitive Newtonian creep, *Acta Mater.*, *48*, 1517–1531, doi:10.1016/S1359-6454(99)00450-4.

Wang, Z.-C., G. Dresen, and R. Wirth (1996), Diffusion creep of fine-grained polycrystalline anorthite at high temperature, *Geophys. Res. Lett.*, *23*, 3111–3114, doi:10.1029/96GL03077.

White, J., and S. White (1983), Semi-brittle deformation within the Alpine fault zone, New Zealand, *J. Struct. Geol.*, *5*, 579–589, doi:10.1016/0191-8141(83)90070-6.

White, J. C. (1996), Transient discontinuities revisited: Pseudotachylyte, plastic instability and the influence of low pore fluid pressure on deformation processes in the mid-crust, *J. Struct. Geol.*, *18*(12), 1471–1477, doi:10.1016/S0191-8141(96)00059-4.

Zaki, M. (1998), Influence of hydrostatic pressure and multiaxial straining on cavitating superplastic materials, *Metall. Mater. Trans. A*, *29*, 2555–2561, doi:10.1007/s11661-998-0227-6.

Zavada, P., K. Schulmann, J. Konopasek, S. Ulrich, and O. Lexa (2007), Extreme ductility of feldspar aggregates–Melt-enhanced grain boundary sliding and creep failure: Rheological implications for felsic lower crust, *J. Geophys. Res.*, *112*, B10210, doi:10.1029/2006JB004820.

Zelin, M. G., and A. K. Mukherjee (1996), Geometrical aspects of superplastic flow, *Mater. Sci. Eng. A*, *208*, 210–225, doi:10.1016/0921-5093(95)10080-6.

G. Dresen, E. Rybacki, and R. Wirth, GFZ Potsdam, Telegrafenberg D428, D-14473 Potsdam, Germany. (uddi@gfz-potsdam.de)